Monitoring Tidal Currents and Macroturbulence in a High-Flow Tidal Channel Using a Kilometer-Scale Acoustic Travel-Time Instrument

Mahdi Razaz, Len Zedel, Alex E. Hay, and Kiyosi Kawanisi

***Abstract*—A challenge in exploiting tidal energy resources is to determine the most suitable sites for development, and as the industry grows, to monitor the progressive impacts of tidal farms on the flow field and sediment transport regimes. A feasibility experiment was carried out with the fluvial acoustic tomography (FAT) system to assess the combined effects of irregular bathymetry, horizontal and vertical sound-speed gradients, and macroturbulence on the quality of FAT-estimated velocities. The experiment involved reciprocal transmissions at 30-s intervals for four days with two 7-kHz broadband transceivers. To determine the origin and potential interpretive value of the frequent multiple arrivals in the unstratified, highly-turbulent flow conditions, we performed a series of simulations with the Bellhop3D model. We demonstrate that the multiple arrivals mainly arise from out-of-plane sound propagation paths resulting from the effects of the local bathymetry. The maximum mean difference between FAT-estimated currents and the coincident moving-vessel acoustic Doppler current profiler (ADCP) transects is found to be less than 10%. Comparisons are also made between velocity spectra during the full flood and the ebb determined using the FAT velocities and the vertically-averaged velocities from a bottom-mounted ADCP deployed in a later experiment. The spectra exhibit similar shapes in the frequency and wave number overlap regions, indicating that FAT is able to detect macroturbulence. Good agreement is also obtained between the sound-speed estimates based on the travel time and those from *in situ* temperature and salinity data. Overall, the results demonstrate the potential of shallow acoustic tomography for monitoring environmental conditions in high-flow tidal channels.**

***Index Terms*—Acoustic tomography, Bellhop3D, in-stream tidal energy, macroscale turbulence, tidal currents, travel time.**

I. Introduction

While ocean acoustic tomography has been implemented successfully in the deep ocean, it has seen only limited applications in acoustically shallower areas, such as gulfs and straits, despite their great oceanographic interest. Deferrari and Nguyen [1] were among the first who employed acoustic tomography in shallow waters. They used a tomographic instrument to measure the path-averaged currents and temperature in depths less than 400 m and ranges up to ∼45 km in Florida Strait. Overlapping of arrivals, multiple scattering and reflection from the stochastic bottom, and difficulties involved in ray identification were reported to be the key factors that prevented the successful application of the deep ocean tomographic method in shallow water. These difficulties have been explored and overcome—in part through the use of coded pulses and higher frequencies—in the development of the coastal acoustic tomography (CAT) system by Kaneko *et al.* [2] and Zheng *et al.* [3].

In parallel with the CAT development, a subsystem known as fluvial acoustic tomography (FAT) applicable to shallow waters has been under development since 2007 [4]. The FAT system is designed to surmount the complications caused by variability in physical characteristics of the water and the attenuation caused by numerous interactions of the sound with boundaries in very shallow waters. The difference between CAT and FAT lies primarily in the frequency range each system supports, and consequently, the maximum possible separation between source and receiver and the minimum water depth required. FAT emits pulses simultaneously (or sequentially) with a central frequency adjustable in the range of 1–57 kHz. This frequency range covers the mid (1–10 kHz) to high (>10 kHz) frequencies that are often used in shallow water acoustics [5]. Transmitting elements are triggered by a 10-MHz GPS clock with 30-ns rms accuracy for time measurements. The pulse is modulated by a pseudorandom binary m-sequence [6] to suppress noise and to distinguish between near-simultaneous arrivals from different sources. While the submillisecond timekeeping precision allows small separation (∼20 m) between the source and receiver nodes, the maximum separation (∼2.5 km) depends on the order of the m-sequence and frequency of the transmit pulse. In contrast to acoustic velocity meters [7], acoustic scintillation devices [8], and horizontal acoustic

Manuscript received April 7, 2021; revised August 5, 2021 and September 23, 2021; accepted November 4, 2021. Date of publication May 10, 2022; date of current version July 13, 2022. The work of Mahdi Razaz was supported by the Japan Society of the Promotion of Science (JSPS) through the Grants-in-Aid for Scientific Research (KAKENHI) program. The work of Alex E. Hay was supported in part by the ecoEnergy Innovation Initiative program of Natural Resources Canada and in part by the Natural Sciences and Engineering Research Council of Canada. The work of Kiyosi Kawanisi was supported in part by the Japan Science and Technology Agency (Adaptive and Seamless Technology Transfer Program) and in part by JSPS (KAKENHI). *(Corresponding author: Mahdi Razaz.)*

Associate Editor: T. Ross.

Mahdi Razaz was with the Department of Marine Sciences, University of Georgia, Athens, GA 30602 USA. He is now with the School of Ocean Science and Engineering, University of Southern Mississippi, Stennis Space Center, MS 39529 USA (e-mail: mahdi.razaz@usm.edu).

Len Zedel is with the Department of Physics and Physical Oceanography, Memorial University of Newfoundland, St. John's, NF A1B 3X7, Canada (e-mail: zedel@mun.ca).

Alex E. Hay is with the Department of Oceanography, Dalhousie University, Halifax, NS B3H 4R2, Canada (e-mail: alex.hay@dal.ca).

Kiyosi Kawanisi is with the Department of Civil and Environmental Engineering, Graduate School of Engineering, Hiroshima University, Higashi–Hiroshima 739-8511, Japan (e-mail: kiyosi@hiroshima-u.ac.jp).

Digital Object Identifier 10.1109/JOE.2021.3126851

Doppler current profilers (H-ADCPs) [9], FAT transducers are omnidirectional. The use of omnidirectional transducers obviates the need for beam pattern corrections and considerably simplifies the positioning and installation of the transducers.

Recent interest in in-stream hydrokinetic power generation in coastal areas motivates the development of the CAT-type technology for use in high-flow channels. For hydrokinetic technology to become a realistic alternative to conventional energy sources, increased understanding is needed of the effects of flow variability on turbine design and operating life, and on the ecological impacts of turbine-induced changes to the natural flow field. However, we still lack the appropriate tools to assess fully the environmental risks [10] and physical impacts. The CAT-type technology offers a cost-effective alternative that can be used to identify potential sites for development, to control, monitor, and manage currently installed turbines, and as the industry grows, to monitor the progressive physical impacts of an increasing number of turbines. With no requirement to extrapolate vertically to obtain the cross-section average velocity, the shore-based CAT provides path-averaged current readings in its basic form (two acoustic nodes) with uncertainties typically less than 10% when compared to vessel-mounted ADCP [11]–[14]. A significant advantage of the FAT system is that with no need for instrumentation in the middle of the tidal channel, the system does not interfere with navigation, fishing, and recreational activities. Razaz *et al.* [15] deployed an array of eight FAT systems around the perimeter of a meandering part of a shallow river (approximately 3 m deep) characterized by a horizontal gradient of sound speed. Using inversion techniques, they showed that the difference between reconstructed horizontal components of transport and vorticity with stationary ADCP data was less than 20%. In coastal waters, however, higher transmission loss, rough sea surface, air bubble entrainment, and degradation of phase information by turbulence will complicate sound propagation, particularly at the higher frequencies that offer the best velocity resolution. To explore the capabilities of this technology for hydrokinetic applications, this article reports on a feasibility study with one pair of FAT transducers deployed in Grand Passage, NS, Canada. This channel is characterized by highly energetic flows and has been identified as a potential site for hydrokinetic device installations.

II. Reciprocal Sound Transmission in Shallow Waters

In deep ocean tomography, a ray model is typically used to relate the travel time of arrivals to the sound-speed fields averaged over certain depths of the water column [13], [16], [17]. For short-range reciprocal transmission in shallow waters, however, it is often not possible to infer aspects of the structure of sound-speed or current variations as a function of depth. Thus, here, we follow a less restrictive approach assuming all the rays traverse the entire cross-section and review some of the governing equations required for translating the raw reciprocal transmission data into the mean flow velocity.

Reciprocal sound transmission between a pair of colocated sources and receivers allows separating the influence of scalar factors, temperature or salinity, and flow on the effective sound speed. Using $\pm$ signs to denote the sound propagation in opposite directions, the one-way travel time t_i for ray path *i* with a length of Γ_i takes the form

$$t_i^{\pm} = \int_{\Gamma_i^{\pm}} \frac{\mathrm{d}\psi}{c(\psi,\tau) \pm \mathbf{u}(\psi,\tau)\cdot\mathbf{n}_i} \tag{1}$$

where $\mathrm{d}\psi$ is the increment of length along the ray path and $c(\psi,\tau)$ is the sound speed along the path at the time of pulse transmission τ, $\mathbf{u}(\psi,\tau)$ is the current velocity, and $\mathbf{n}_i$ is a unit vector tangent to the ray path. Given that $|\mathbf{u}| \ll c$, (1) can be linearized, and the difference between the travel times in the forward and reverse directions becomes

$$\Delta t_i = t_i^{+} - t_i^{-} = -2\int_{\Gamma_i^{\pm}} \frac{\mathbf{u}(\psi,\tau)\cdot\mathbf{n}_i}{c(\psi,\tau)^2}\mathrm{d}\psi \tag{2}$$

assuming the reciprocity assumption is valid, i.e., sound travels along the same path in each direction. Given the small depth to width ratio, we further assume that the ray length does not change with the tide and is comparable to the horizontal distance between the source and receiver, i.e., $\Gamma_i^{\pm} = \Gamma \approx L$. Given that sound-speed variations along the path $\delta c(\psi,\tau)$ are much smaller than the path-averaged sound speed, c_m, $c(\psi,\tau)$ in (2) can be replaced by c_m, and the integration carried out to obtain the path-averaged current, $u_m(\tau)$, which yields

$$u_m(\tau) \approx -\frac{c_m(\tau)^2}{2\Gamma}\Delta t_i. \tag{3}$$

In addition, the mean sound speed can be related to the average time-of-flight through

$$c_m(\tau) = \frac{\Gamma}{2}\left(\frac{1}{t^+} + \frac{1}{t^-}\right) \approx \frac{\Gamma}{t_m} \tag{4}$$

where t_m is the average of the travel times in the forward and reverse directions in each simultaneous transmission. The resulting values of c_m are used in a later section to estimate the water temperature averaged over the width of the channel.

III. Survey Site and Hydrographic Measurements

Grand Passage is located at the mouth of the Bay of Fundy, on the south side (see Fig. 1). It is about 1 km wide and 4 km long. In the channel, currents are primarily induced by semidiurnal tides and were as high as 1.7 m/s during the observation period. With an average tidal range of 5 m, the maximum water depth in the channel was approximately 30 m at high water. The high flow speeds and shallow bathymetry make Grand Passage a suitable site for small-scale tidal energy development [18] and it has been selected as a site for in-stream tidal power development under the Nova Scotia community feed-in tariff program.

Two ITC 2003 broadband transducers with a source level of 190 dB re 1 μPa at 7-kHz central frequency were attached to wharves on the Westport and Freeport sides of Grand Passage—marked as WP and FP in Fig. 1. In strongly stratified estuaries, the depth of the transducers relative to the thermocline/pycnocline must be carefully chosen to prevent entrapment of the sound in either a surface or bottom duct. Here, because of

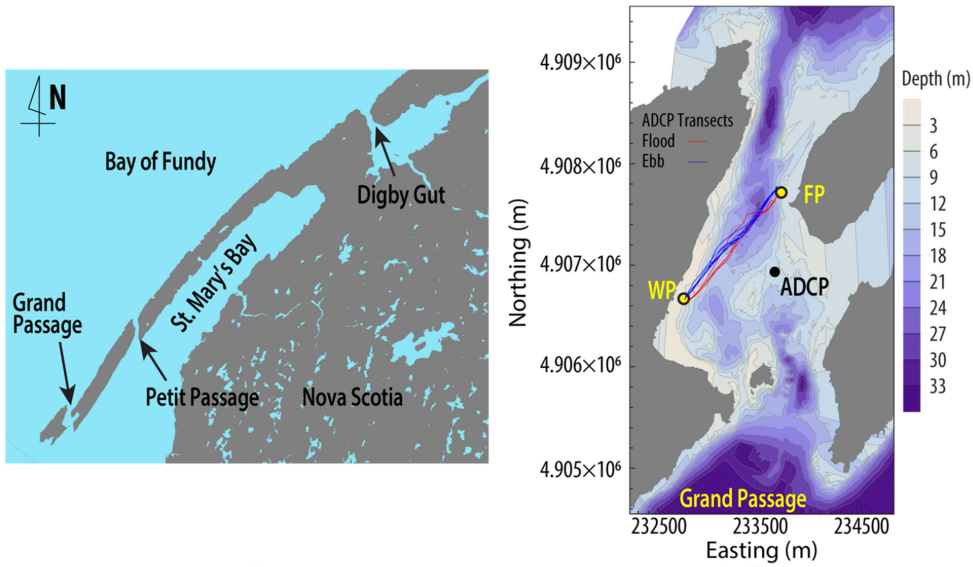

Fig. 1. (a) Map of Digby Neck, NS, Canada. (b) Bathymetry of the survey site, Grand Passage, together with the WP (44° 16' 27.78" N, 66° 20' 8.66" W) and FP (44° 15' 50.34" N, 66° 20' 52.8" W) stations where FAT transducers and TP sensors were positioned. Coordinates are referenced to the WGS84/UTM20 system. The black dot in (b) denotes the location of the stationary ADCP and red (blue) lines denote the moving-vessel ADCP track during the flood (ebb).

TABLE I
TRANSMISSION SIGNAL PARAMETERS

Carrier central frequency	7 kHz
Carrier bandwidth	2.5 kHz
Order of m-sequence	10
Processing gain	30.1 dB
Sequence length	1023 digits
Cycles per digit	3
Digit duration	0.428 ms
Pulse duration	0.438 s
Number of pulses	1

the homogeneity of the water column, the only restriction was the tidal range. Thus, near the shore where the water depth is much less than the central parts of the channel, the transducers were positioned below the low water mark and as close as possible to the bed (about 1 m above the bed) at a horizontal separation of 1502 m. A SCUBA diver secured the transducers such that their motion was constrained to be less than 0.5 m in any direction. Reciprocal sound transmissions were performed with 30-s intervals during August 28–31, 2014. The properties of the source signal are briefly listed in Table I.

The power of modern vessels using diesel engines means significant levels of both low- and high-frequency noise are radiated underwater. A study performed by the International Council for the Exploration of the Sea (ICES) aiming at measuring underwater noise of research vessels suggests that noise at frequencies (O(10 kHz)) [19] that might degrade FAT performance is primarily generated by propellers. In Grand Passage, a ferry sailed every half hour along a path close to the WP–FP line. The duration of each crossing was less than 10 min. There are no crossings at night. The noise from the 39-m, 100-passenger ferry with dual 365-BHP diesel engines driving fore-and-aft propellers [20] would make noise levels (approximately 120 dB re 1 μPa at 10-kHz) [19] comparable to a hydrokinetic turbine [21]. A discussion of FAT signal-to-noise ratios (SNRs) is given in Section IV.

A. *Variability of Salinity and Temperature*

Ancillary physical water column data including conductivity, temperature, and depth (CTD) profiles were gathered from Sontek CastAway CTD casts scattered along the general transmission path. Presented in Fig. 2(a) are the temperature data, averaged over each pair of down- and up-casts collected on August 28 and 30, 2014. We used the Gibbs-SeaWater (GSW) Oceanographic Toolbox [22], part of the Thermodynamic Equation Of Seawater 2010 (TEOS-10) [23], to calculate the absolute salinity profiles exhibited in Fig. 2(b). The upper 5 m of the water column was noticeably less saline and warmer during the ebb. Aside from this surface layer during the ebb, the temperature profiles remain more or less uniform over the rest of the water column due to the strong tidal mixing, varying with the tide over the narrow range of 12.4 °C–13.9 °C. The variability of salinity with depth, except near the surface, is negligible, compared to that associated with the ebb and flood tide (∼1.4 g/kg). The GSW Oceanographic Toolbox was used to compute sound-speed c_{ST} profiles from the observed temperature and salinity [see Fig. 2(c)]. The sound-speed profiles are weakly upward refracting with a mean value showing a strong correlation with

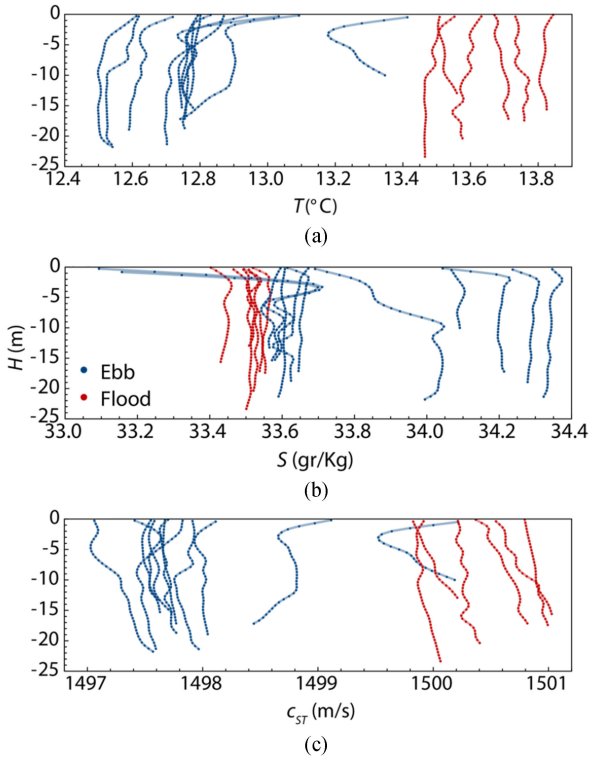

Fig. 2. Profiles of (a) temperature, (b) absolute salinity, and (c) the corresponding sound speed from CastAway CTD casts along the WP–FP line [see Fig. 1(b)] on August 28 and 30, 2014. All profiles are averaged over each pair of down and up casts.

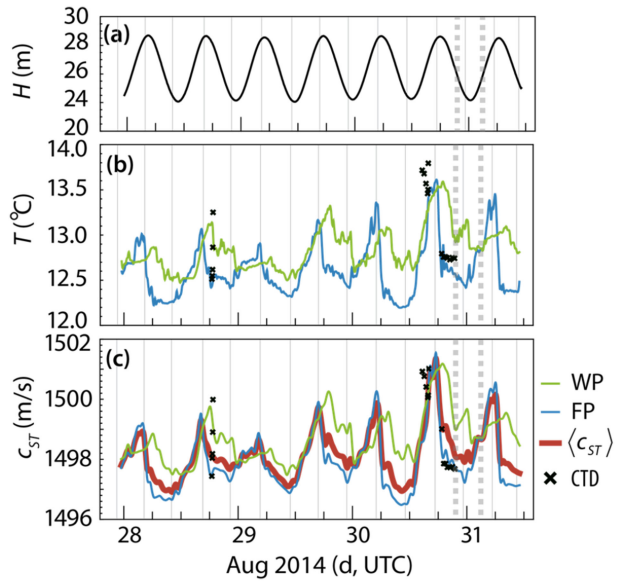

Fig. 3. (a) Relative water level referenced to the deepest point of the cross-section between WP and FP stations. (b) Temperature at FP and WP stations close to the FAT transducers. The ×'s indicate the depth-averaged temperature data from CTD casts approximately along the WP–FP line. (c) Reference sound-speed $\langle c_{ST} \rangle$ determined using the weighted mean temperature and a constant absolute salinity of 33.5 g/kg. The vertical gridlines denote times of flow reversal. The dashed lines denote the times at which TP data were used in Bellhop3D simulations (see Section V).

the tidal phase, i.e., typically the sound speed during the flood was 3 m/s higher than the ebb.

In addition to the discrete CTD profiles in deeper parts of the channel, RBRduo temperature–pressure (TP) sensors were positioned close to each transducer to register time-series data at a sampling rate of 6 Hz. Fig. 3 demonstrates the tide-induced fluctuations in pressure (referenced to the deepest point between WP and FP) and temperature as a function of time during the campaign. Also shown are the depth-averaged CTD data. Due to the spatial separation between the TP sensors and the CTD casts as well as different sampling methods, the two sets of data do not agree perfectly. Section-average temperature, $\langle T(\tau) \rangle = 0.3T_{\mathrm{WP}}(\tau) + 0.7T_{\mathrm{FP}}(\tau)$, was computed from the TP sensor data. This time-varying temperature, in combination with a constant salinity, $S = 33.5$ g/kg obtained by averaging all CTD profiles [see Fig. 2(b)], was used to calculate sound-speed $c_{ST}(\tau)$ using the GSW toolbox. The weights were estimated based on the distance of each of the TP sensors from a temperature front along the WP-FP line, which will be described in Section III-B. Angle brackets denote section average values. The assumption of depth- and time-independent salinity represents a maximum error of approximately 1 m/s in the sound-speed estimations.

B. Vessel-Mounted ADCP Measurements

Concurrent with the acoustic measurements, 11 transects were made (4 during the flood and 7 in the ebb) on August 30, 2014, using a vessel-mounted 1200-kHz TRDI Workhorse ADCP recording single-ping data at 1 Hz in 0.2-m-range bins in the TRDI mode 1. To keep the boat on the transmission path as much as possible, during the flood, the transects started from station WP and during the ebb from station FP. All the transects started and ended within a few meters of the transducers. Any drift in the bottom track positions due to compass error was corrected using the coordinates registered by a handheld GPS device. The current data were referenced to the ADCP bottom track velocities.

While the longer and more powerful bottom tracking pings could reach the deepest parts of the cross-section, the velocity profiling range was limited to 15 m. The flow velocity profiles were reconstructed using the log-law [24], [25] that is a standard model for boundary layer structure. The velocity profiles were also smoothed spatially using the inverse distance weighting (IDW) interpolation method [26]. For a given range cell, all the data within 5 single-ping profiles in the horizontal direction (the actual distance varies with the boat speed) and 1.6 m (8 range cells) in the vertical direction are included in the averaging. Exhibited in Fig. 4(a) are two representative ADCP transects of flow distribution in the flood and the ebb, after smoothing. Positive values denote currents during the ebb, toward the south; negative values correspond to currents during the flood, toward the north.

During the ebb, the headlands on the eastern side of the channel and the associated shoal extending from the shoreline (see Fig. 1) cause flow separation and subsequent generation of vorticity. During the flood, smaller eddies are generated

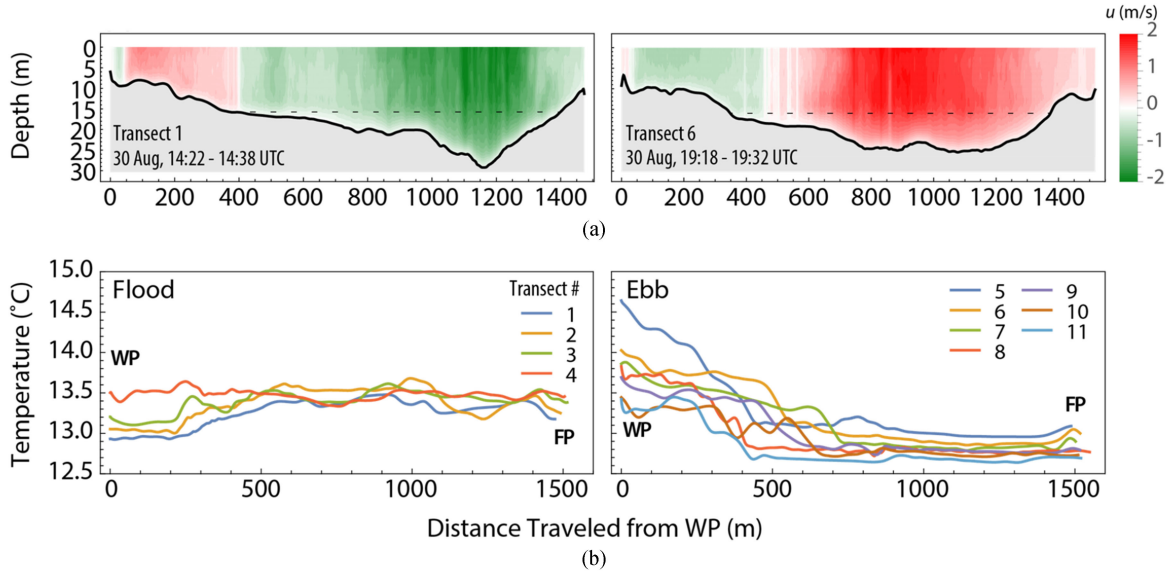

Fig. 4. Vessel-mounted ADCP results. (a) Top row presents two samples of the flow magnitude distribution along the boat track for the flood (left) and the ebb (right). Transects are extrapolated beyond 15 m (indicated by dashed lines) for presentation purposes (Section III B). Positive values denote ebb currents (toward the south), whereas the negatives stand for the flood currents (toward the north). (b) Bottom row is the near-surface temperature from all transects.

by the ridge extending from the west together with the small island at the southern entrance to the channel. The eddy formed close to the western shoreline (station WP) was stronger. The temperature data recorded by the ADCP presented in Fig. 4(b) denote a marked difference between values inside and outside the shoreline-trapped eddy on the WP side. Comparing the surface temperature data with the TP records shown in Fig. 3(b) provides further evidence that the formation of a temperature front in association with two shoreline-trapped eddies [countercurrents in Fig. 4(a)] was a persistent feature of the flow structure in all the ADCP transects (not shown here). Whether the water in the shoreline-trapped eddy to the west of this front is colder or warmer compared to the rest of the channel depends on the tidal phase. The temperature contrast is more pronounced during the ebb than during the flood (see Fig. 4). The edge of the front is about 450 m from WP, measured along the WP–FP line. This distance is used to roughly estimate the weights used in section-average temperature calculations.

The mean flow direction, with respect to true east, from the ADCP transects was obtained via

$$\langle\theta_{\mathrm{ADCP}}\rangle = \tan^{-1}\left(\sum_{i}^{P}\sum_{j}^{B} v_{N_{ij}} \Big/ \sum_{i}^{P}\sum_{j}^{B} v_{E_{ij}}\right) \quad (5)$$

where v_E and v_N are, respectively, east and north velocity components, P is the number of pings in each transect, and B is the number of range cells with good data in ping i. The section-averaged flow direction was estimated to be $\langle\theta_{\mathrm{ADCP}}\rangle_{\mathrm{Flood}} = 108.7^\circ \pm 1.1^\circ$ and

$$\langle\theta_{\mathrm{ADCP}}\rangle_{\mathrm{Ebb}} = 250.3^\circ \pm 7.8^\circ.$$

The corresponding mean velocities were obtained by averaging the profiles weighted by the distance traveled by the vessel without taking into account the missing portions.

C. Bottom-Mounted ADCP Measurements

As part of a later experiment carried out in the spring of 2016, a Nortek Signature 500 ADCP, mounted in an upward-looking orientation within a heavily ballasted frame, was deployed on the seabed at the location indicated in Fig. 1(b), with the ADCP center transducer 0.8 m above the bottom. Beam coordinate velocities were recorded continuously on all 5 beams in 0.5-m vertical range bins at a sampling rate of 2 Hz. The range to the first bin was 1 m. The duration of the deployment was 25.8 d. In a later section of the article, the spectra of the vertically-averaged velocities from this single-point ADCP record are compared to the spectra of the channel-averaged velocity estimates obtained from the acoustic tomography system.

IV. Travel Times

Given the first estimates of sound speed and known source–receiver distance, we were able to approximate the arrival time. A window with a length of 32 ms was determined to record each received signal. The onset is selected such that the window opens several ms before the expected first arrival; the length of the window depends on the environmental conditions and the expected sound-speed variability. Acoustic arrival times were calculated by taking the cross-correlation of the received signal with a replica of the transmitted signal [2]. These cross-correlations provide output values that are somewhat analogous to SNR but in arbitrary units that depend on the code length and scaling used. To identify the stable arrival times, an in-house pattern recognition algorithm was developed. In the first step, the algorithm identifies up to five significant peaks in the entire length (32 ms) of signal correlations recorded. This step was implemented for the data collected at each station independently and only selects peaks associated with SNR ≥ 9. Step 2 pairs the peaks detected in step 1 using a 15-ms search window while

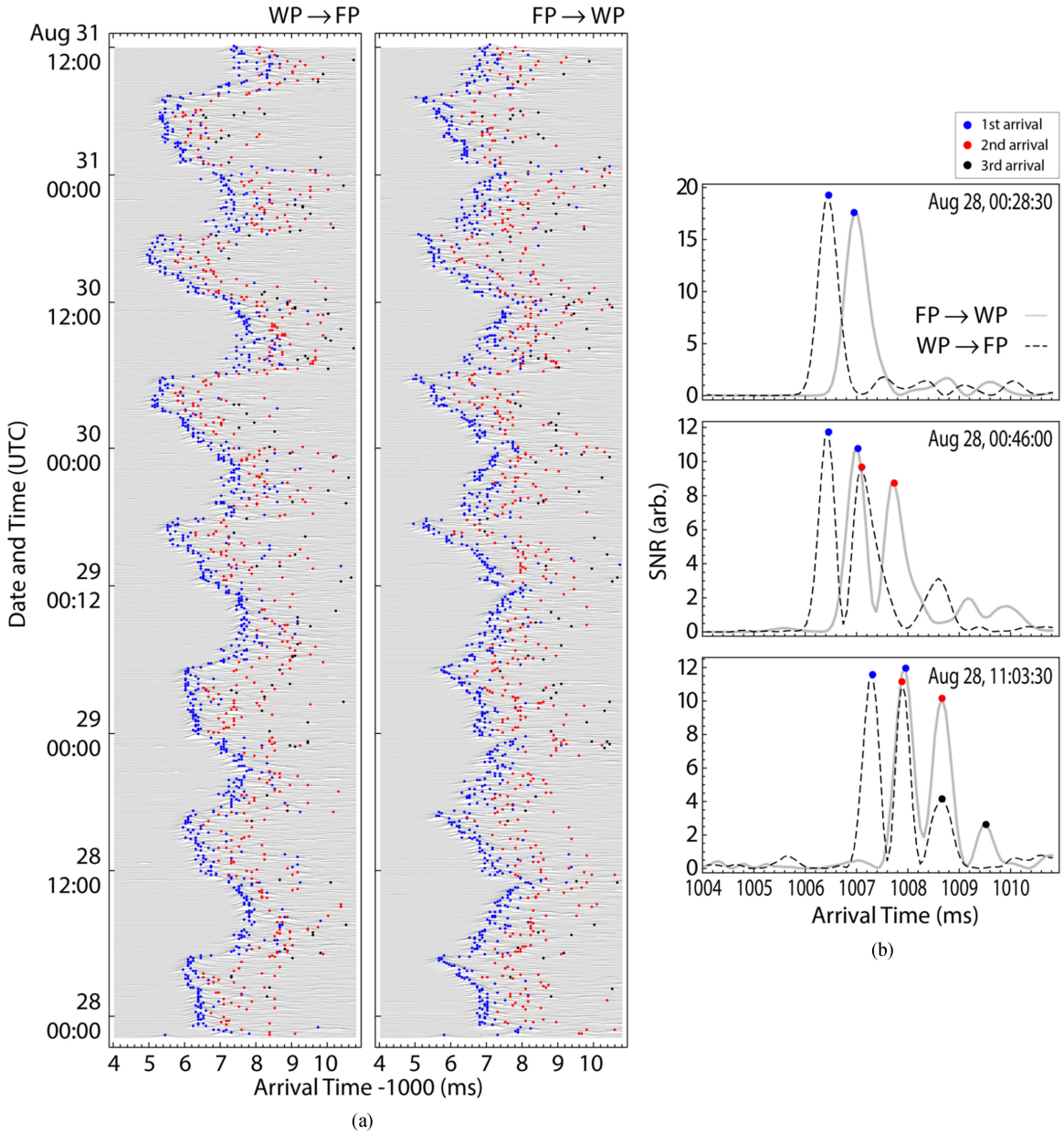

Fig. 5. (a) Every 30th (15 min) cross-correlation of the recorded signals with the corresponding transmit replica over the deployment period for the two opposite acoustic transmission paths. (b) Samples of the signal correlations without any averaging. The colored dots denote the order of arrival: i.e., blue, first; red, second; and black, third.

taking into account the relative flow direction and SNR. The window is centered at the peak with higher SNR regardless of the direction of sound transmission. Note that $\Delta t = 7.5$ ms corresponds to path-averaged currents as large as 5 m/s. Considering the average observed currents are less than 2 m/s (see Fig. 4), the length of the window ensures the identification of all potential pairs of peaks. If any *orphan* peak remains, the algorithm searches for a counterpart with a SNR threshold now reduced to 3. Both thresholds used for peak detection are chosen based on hardware and environmental conditions to report approximately 95% of all the possible peaks detected in reciprocal directions. Any peaks that would correspond to an orphan arrival time remaining after the last step were rejected. We further dropped peaks 4 and 5 due to sparsity and their stochastic appearance in the data. Examples of the first three consistent arrival times identified utilizing this approach for single reciprocal transmissions together with the results for the entire campaign period are demonstrated in Fig. 5. The arrival times are evidently modulated by variations in the sound-speed field induced predominantly by temperature advection due to the tide. The earliest and latest arrivals are associated with high and low water, respectively, and are due predominantly to the variations in temperature (see Fig. 3). The arrival times are seen to spread over approximately 7 ms after the first arrival (from 1004 to 1011 ms in absolute time) in both directions. The first two arrivals had persistently higher signal levels

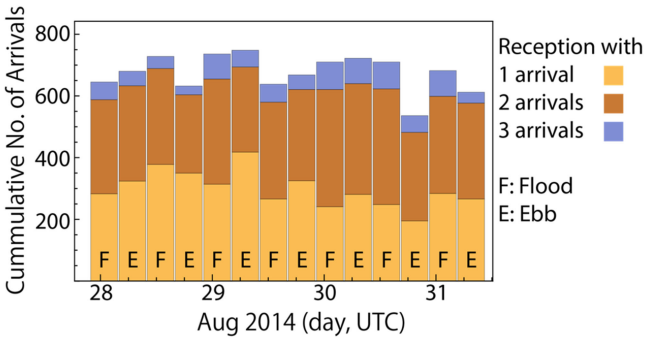

Fig. 6. Cumulative number of successful reciprocal transmissions in each tidal phase over the observation period. Colors denote the number of arrivals.

[see, e.g., Fig. 5(b)] and were more stable and temporally consistent than the later-arriving portions of the signal. No systematic noise signature that can be attributed to the passage of the ferry is indicated in the SNRs—SNR time-series corresponding to each group of arrivals are not shown here.

Overall, 51.4% of the successful reciprocal transmissions were performed during the flood (the span between successive flow reversals), and the remaining 48.6% during the ebb. Mean flow speeds and turbulence intensities in Grand Passage exhibit pronounced flood/ebb asymmetry, the sense of which varies with position in the channel [27]. The difference in turbulence intensity levels in the flood and the ebb, however, does not seem to affect the cumulative number of successful reciprocal transmissions regardless of the number of arrivals, as shown in Fig. 6.

A. *Differential and Mean Travel Times*

The use of colocated sources and receivers allows us to form the travel time differences, WP-to-FP minus FP-to-WP, which, in the linear approximation, depend only on the current component along the transmission path. The low-pass filtered (5-min cutoff) differential travel times Δt and average travel times t_m are shown in Fig. 7. The cutoff is selected based on the power spectra of Δt time series to remove the noise floor. Semidiurnal oscillations in Δt and t_m are evident for all three groups of arrivals. The cross-correlation between t_m and the TP temperature records indicates a negative peak with 113- and 15-min lags for the WP and FP stations, respectively. The longer lag associated with the WP station is due to the formation of the shoreline-trapped eddy on the WP side.

The potential role of horizontal shear as a cause of multiple arrivals was investigated by examining the intermultiple travel time differences since shear might lead to alteration of arrival times in opposite directions differently. To do so, time-ordered sequences, δt_{WF} and δt_{FW}, were formed from the differences between successive arrivals. For WP→FP path, δt_{WF} consists of $t^{(2)}_{\mathrm{WF}_i} - t^{(1)}_{\mathrm{WF}_i}$ and $t^{(3)}_{\mathrm{WF}_i} - t^{(2)}_{\mathrm{WF}_i}$, where $t^{(n)}_{\mathrm{WF}_i}$ is the nth arrival time in the ith transmission. δt_{FW} can be calculated likewise. Fig. 8 compares δt_{WF} and δt_{FW}. Overall, δt_{FW} and δt_{FW} are correlated through $\delta t_{\mathrm{WF}} = 0.95\,\delta t_{\mathrm{FW}} \pm 0.62$ ($R^2 = 0.81$), indicating that shear did not significantly affect the sound propagation and was not responsible for multiple arrivals.

The reciprocity required for the linearization of (1) can be tested by examining the high-frequency travel time variances. If the oppositely directed paths were truly reciprocal, they would see the same sound-speed field, and high-frequency fluctuations would be canceled in the travel time difference. However, the degree of cancellation is reduced predominantly by sound-speed perturbations, refraction by current shear, ambient noise, random movement of the transducers, etc. To remove fluctuations attributable to transducer motion and processing error, the arrival time data were bandpass filtered with cutoff frequencies ($2.8\times10^{-4} \leq f(\mathrm{Hz}) \leq 0.5\times10^{-3}$) based on power spectra computed for flood and ebb velocities described in Section VII. The one-way variances of bandpass-filtered travel-time fluctuations, for the first arrivals are 0.11 ms^2, whereas the variance of the differential travel times is 0.08 ms^2. If the high-frequency variabilities of reciprocal transmissions were uncorrelated, the variance of the differential travel times would be twice that of the one-way travel times [28]. The corresponding correlation-coefficient for the bandpass-filtered travel times in reverse directions, $t^{(1)}_{\mathrm{WF}}$ and $t^{(1)}_{\mathrm{FW}}$, is 0.62. This means that the oppositely directed ray paths are sufficiently close spatially to see nearly the same sound-speed field and large-scale shears do not significantly perturb the ray paths.

V. Bellhop Simulations

The Bellhop3D model [29], [30] was used for acoustic modeling as, in contrast to the standard Bellhop (2-D environment), it allows for spatial variability of sound-speed and out-of-plane ray paths. Without direct detailed measurements of salinity and temperature throughout the campaign, it was not possible to establish a precise 3-D sound-speed field for the channel. One method, albeit a compromise, is to construct a general profile that includes the main characteristics of the sound-speed field. To do so, the sound-speed profile was decomposed into the vertical average $\bar{c}$ and perturbation $\delta c(z)$ components. The perturbations indicated in Fig. 9(b) were obtained by averaging the CTD profiles [see Fig. 2(c)] over the tidal phase at each corresponding normalized depth z/H after removing the mean, where z is the depth of measurement and H is the water depth. The average sound-speed inside and outside of the frontal zone was computed using the $\mathrm{TP_{WP}}$ and $\mathrm{TP_{FP}}$ temperature records, respectively, together with a constant salinity (33.5 g/kg.) The vertical sound-speed profiles were defined in the Bellhop3D model in a 25×25-m horizontal grid [shown in Fig. 9(a)] with 1-m depth intervals, the finest horizontal and vertical resolutions allowed by the model.

In the geometric mode, Bellhop3D simulates the propagation of a fan of ray tubes that trace the paths of points normal to propagating wavefronts. The widths of the fan in the horizontal $\hat{\theta}_{XY}$ and vertical $\hat{\theta}_{XZ}$ planes must be specified together with the corresponding number of ray tubes in each plane. In this work, the fan width in the vertical plane was kept constant for all cases at $-20° \leq \theta_{XZ} \leq 20°$; to examine the effect of launch angle on

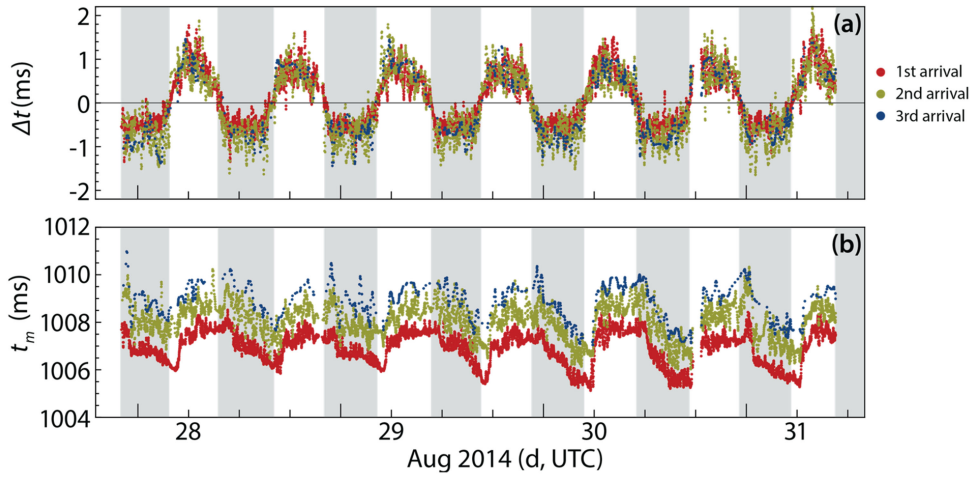

Fig. 7. (a) Differential and (b) mean travel times for all the three groups of identified arrivals in FAT records. Periods of flooding tide were assigned negative values and periods of the ebbing tide were assigned positive values. The gray shades denote flooding tide.

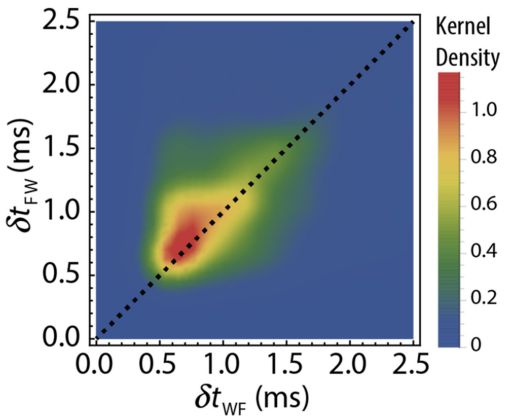

Fig. 8. δt_{WF} against the corresponding values of δt_{FW} shown to illustrate the effect of horizontal shear on multiple arrivals. The dashed 1:1 line is included for reference.

TABLE II
SUMMARY OF THE BELLHOP3D SIMULATION CASES

	Description	Horizontal fan width (deg)	c_{ST} inside/outside of the front on WP side (m/s)	Maximum δc_{ST} in the vertical profile (m/s)
Case 1-A	Typical ebb	-5 to +5	1499.1 / 1497.7	0.3
Case 1-B	Effect of horizontal fan width on the out-of-plane scatter	-0.5 to +0.5	1499.1 / 1497.7	0.3
Case 2	Pure effect of bathymetry on the out-of-plane scatter	-5 to +5	1498.1 / 1498.1	0.0
Case 3	Effect of horizontal sound-speed gradient on the out-of-plane scatter	-5 to +5	1498.1 / 1495.7	0.3
Case 4	Effect of vertical sound-speed gradient on the out-of-plane scatter	-5 to +5	1499.1 / 1497.7	0.6
Case 5	Typical flood	-5 to +5	1498.6 / 1498.6	0.8

the out-of-plane propagation, uniform beams within

$$\textit{narrow}\ \hat{\theta}_{XY} = 1^{\circ}(-0.5^{\circ} \leq \theta_{XY} \leq 0.5^{\circ})$$

and

$$\textit{wide}\ \hat{\theta}_{XY} = 10^{\circ}(-5^{\circ} \leq \theta_{XY} \leq 5^{\circ})$$

sectors were implemented. Positive grazing angles denote rays launched toward the surface. The azimuthal angle is referenced to the WP–FP line with the positive values denoting rays launched toward the north. We found that rays launched outside the wide horizontal fan interacted with the boundaries numerous times, but did not contribute to the overall results. The density of ray tubes was kept constant at 250/degree in both horizontal and vertical fans. In all cases, the sound was emitted from the WP station (1.9 mbsl) and received at the FP station (2.7 mbsl), separated by 1502 m horizontally. The transmit frequency was set to 7 kHz with each individual ray tube having a Gaussian beam shape. Rays with more than 20 interactions with the surface and bottom were neglected.

Bellhop3D also allows the user to specify the geoacoustic properties of the bottom. Since these properties are not well known for Grand Passage, they were roughly estimated by assuming typical values of $\rho_g = 2.73$ g/cm^3 for the grain density and an average grain size of 0.4 mm [31]. Following Buckingham [32] and Hamilton [33], [34], compressional and shear wave speeds were approximated as $c_P = 1700$ m/s and $c_S = 160$ m/s with corresponding attenuation coefficients of $\alpha_P = 2$ dB/m and $\alpha_S = 178$ dB/m for a bottom with 2.1 g/cm^3 density. (Here, the subscripts P and S denote, respectively, the compressional and shear waves.) Transmission loss and attenuation due to the interaction of sound with sea surface roughness were not taken into account in the simulations.

We ran Bellhop3D trials for different environmental conditions (see Table II). Case 1-A is an attempt to hindcast the sound propagation in the channel during the ebb; hence, the corresponding TP records (marked on Fig. 3) were used to estimate the sound-speed profiles inside and outside the frontal

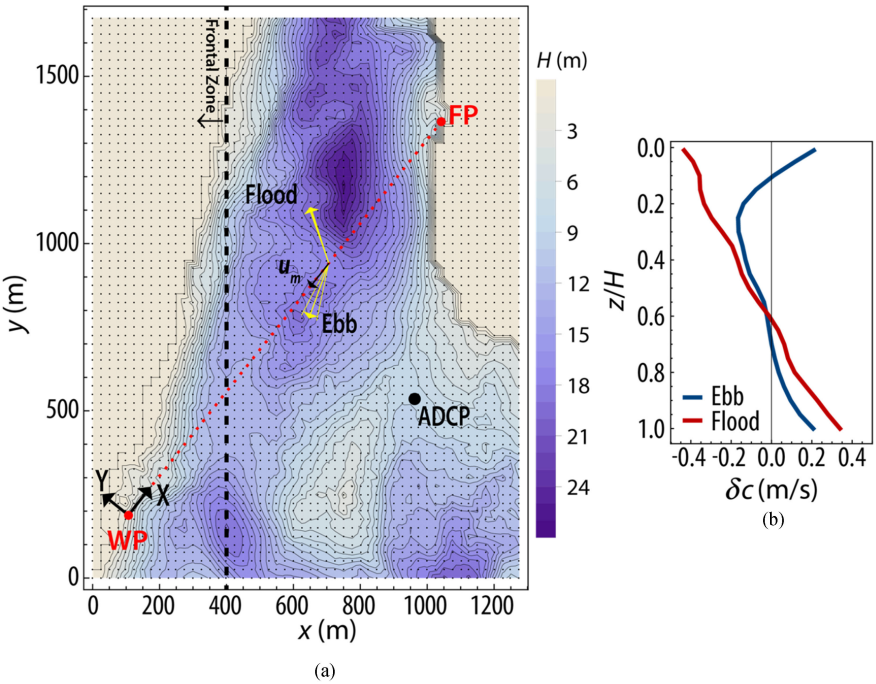

Fig. 9. (a) Plan view of the Bellhop3D simulation domain. The bathymetry is based on multibeam sonar surveys with a horizontal resolution of about 2 m. The source (WP) and receiver (FP) were positioned, respectively, at 1.9 and 2.7 mbsl and 1502 m apart: i.e., the values for the *in situ* instruments. The thick dashed line roughly denotes the temperature front formed on the WP side. The distance between WP and the front along the WP–FP line is approximately 450 m. The small black dots indicate the grid nodes at which bathymetry and sound-speed data were defined in the model. The mean current directions during the flood and the ebb and the corresponding ± 1 SD range obtained from 11 ADCP transects are also shown. The large black dot indicates the location of the bottom-mounted ADCP. (b) Vertical profiles of sound-speed perturbations for the flood and the ebb as a function of normalized depth.

zone illustrated in Fig. 9(a). To explore the sensitivity of out-of-plane sound propagation to the horizontal fan width, case 1-A is repeated in case 1-B but with a narrow horizontal fan width. In case 2, the sound-speed field was uniform to explore the effects of bathymetry alone on the sound propagation pattern. A constant salinity (33.5 g/kg) together with a uniform temperature calculated from $\langle T(\tau)\rangle = 0.3T_{\mathrm{WP}}(\tau) + 0.7T_{\mathrm{FP}}(\tau) = 12.7\,^{\circ}\mathrm{C}$ was used to estimate the sound speed. Case 3 investigates the effect of a horizontal gradient of sound speed on multiple arrival patterns. The sound speed outside the frontal zone, on the FP side, is reduced by 2 m/s, whereas the sound speed inside the front is kept the same as case 1-A to create a stronger horizontal gradient. Likewise, to examine the effect of nonuniform sound-speed in the vertical, δc was increased to 0.6 m/s, twice that indicated by Fig. 9(b), in case 4 with $\bar{c}$ calculated from the TP records. The last case, case 5, is the same as case 1-A but in the flood. Sound-speed perturbations shown in Fig. 9(b) along with the mean values calculated from the corresponding TP records (marked on Fig. 3) were used to reconstruct the basic features of the sound-speed field.

A. *Causes of Multiple Arrivals*

Projections of 3-D eigenrays shown in Fig. 10 are referred to a set of rectangular Cartesian axes *X*, *Y*, and *Z* whose origin is located on the free surface above the WP station [see Fig. 9(a)] with *Z* measured vertically downward, $Z = H$ denotes the seafloor. In the *XZ*-plane, as shown in Fig. 10(a), only minor changes in the sound propagation pattern occur when the sound-speed structure varies vertically, e.g., compare case 1-A with case 4. Of more interest in Fig. 10 is the stability of the three distinctive ray bundles that are formed in the *XY*- and *XZ*-planes across all the scenarios. The consistency of recovering three arrivals in simulations implies that Bellhop spatial resolution is adequate and the results contribute to our understanding of the observations. Relative density of rays (see Figs. 10 and 12) indicates that the rays forming the first arrivals (the bundle with the least deviation in the *XY*-plane) traverse roughly the entire cross-section, whereas the second and third arrivals propagate along distinctive paths and thus sample the cross-section nonuniformly. These paths seem to be stable and do not change with the tidal phase.

The corresponding arrival time probability density functions (PDFs) are displayed in Fig. 11. The PDFs are weighted using the inverse number of interactions each ray makes with the surface and bottom boundaries as a proxy for sound attenuation; the earliest arrival time in each case is subtracted to give the arrival lag. It is noted that the Bellhop3D travel time predictions are on average about 3 ms ($\sim$5 m) shorter than the FAT observations. This difference may arise from the error in measuring the distance between WP and FP stations, a paucity of sound-speed measurements in space and time, and/or the resolution (25×25 m) of the model that requires smoothing of the bathymetry. For each PDF, arrival times of the simulated rays are shown as a function of their standard deviations from the WP–FP line in the *XY*-plane, SD_Y. The number of interactions with surface and bottom boundaries is denoted by color. Each pair of figures should be viewed together. In all simulated cases,

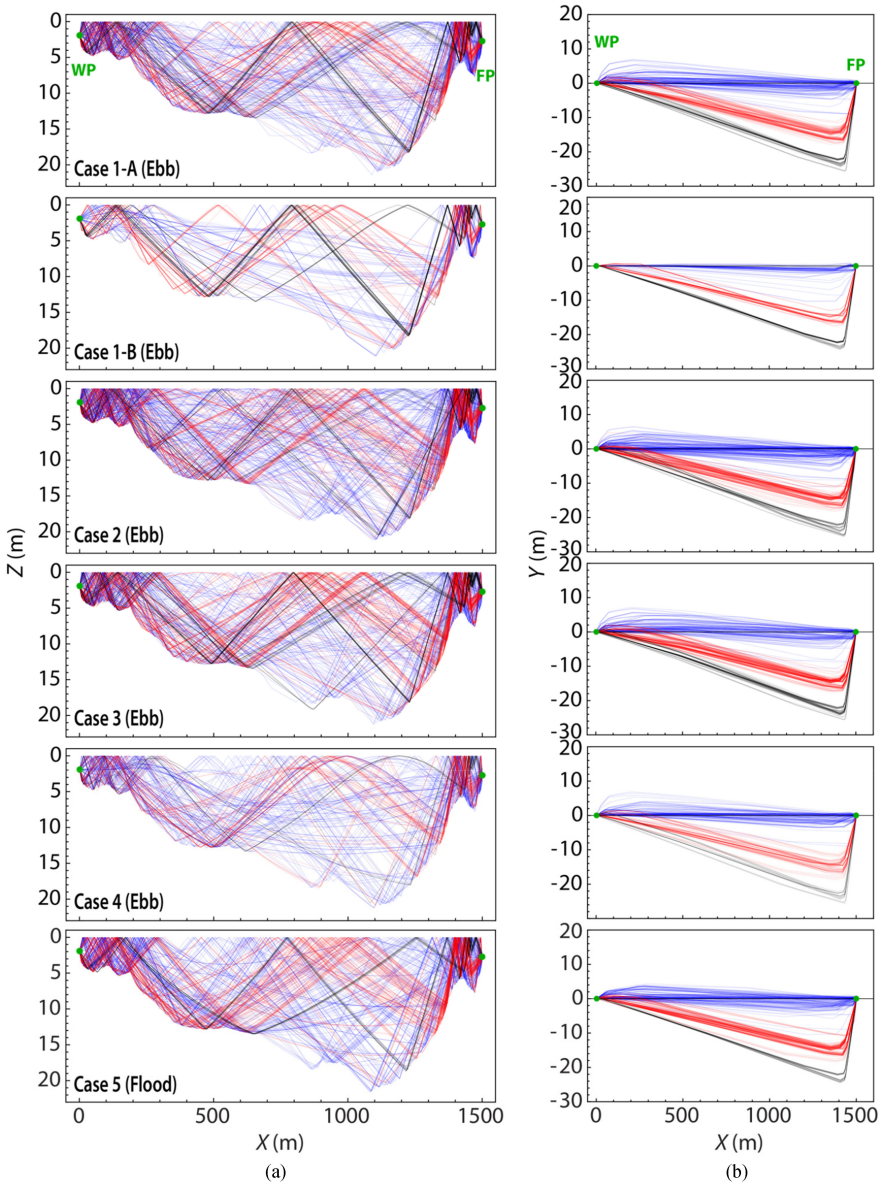

Fig. 10. Bellhop3D ray-tracing results. (a) Projections onto *XZ*- and (b) *XY*-planes indicating how acoustic beams travel through the channel for the different cases summarized in Table II. Notice how the three ray bundles in the *XY*-plane remain unchanged. The largest launch angle associated with an eigenray rarely deviates more than 1° from the WP–FP line.

the data accumulate into three distinct clusters, in each, the number of interactions rays make with boundaries increases with time lag. It is evident that if only rays with small SD_Y values are considered (as in 2-D space), there would be only one distinct arrival bundle demonstrating that the occurrence of multiple arrivals requires the use of 3-D modeling. Nevertheless, considering that FAT treats the acoustic reception as a group of multipath signals having the same arrival time, in each cluster, the contribution of rays with fewer interactions will dominate contributions to the peak of the PDFs shown. Thus, although there are overlaps between the three clusters in time, as shown by the color codes in the PDFs, considering the density of rays, three distinct arrival groups are evident. Overall, Fig. 11 implies that the arrival time should not be the sole criterion for grouping the rays. That is, multiple arrivals are formed by out-of-plane propagation and the number of interactions with boundaries and, therefore, the lengths of the rays. The structure of the density of rays in the *XZ*-plane (shown in Fig. 12) supports this argument by indicating that the three stable ray paths, each associated with one of the clusters in Fig. 11, only shown for cases 1A (ebb) and 5 (flood), do not vary significantly by sound-speed field.

There are two factors that determine the travel time for a given ray. One is the length of the path traveled between source and receiver. The second is the sound speed along that path. Despite multiple interactions of rays with the boundaries, the relation between the path length and the arrival time is strictly linear due to the well-mixed condition in the channel. Thus, ray length is the primary factor controlling the arrival time. Fig. 13 shows the dependence of ray lengths on θ_{XY}, and θ_{XZ} for different sound-speed fields defined in each simulation case. The distribution pattern of the eigenrays as a function of grazing and azimuthal angles remains nearly unchanged among the

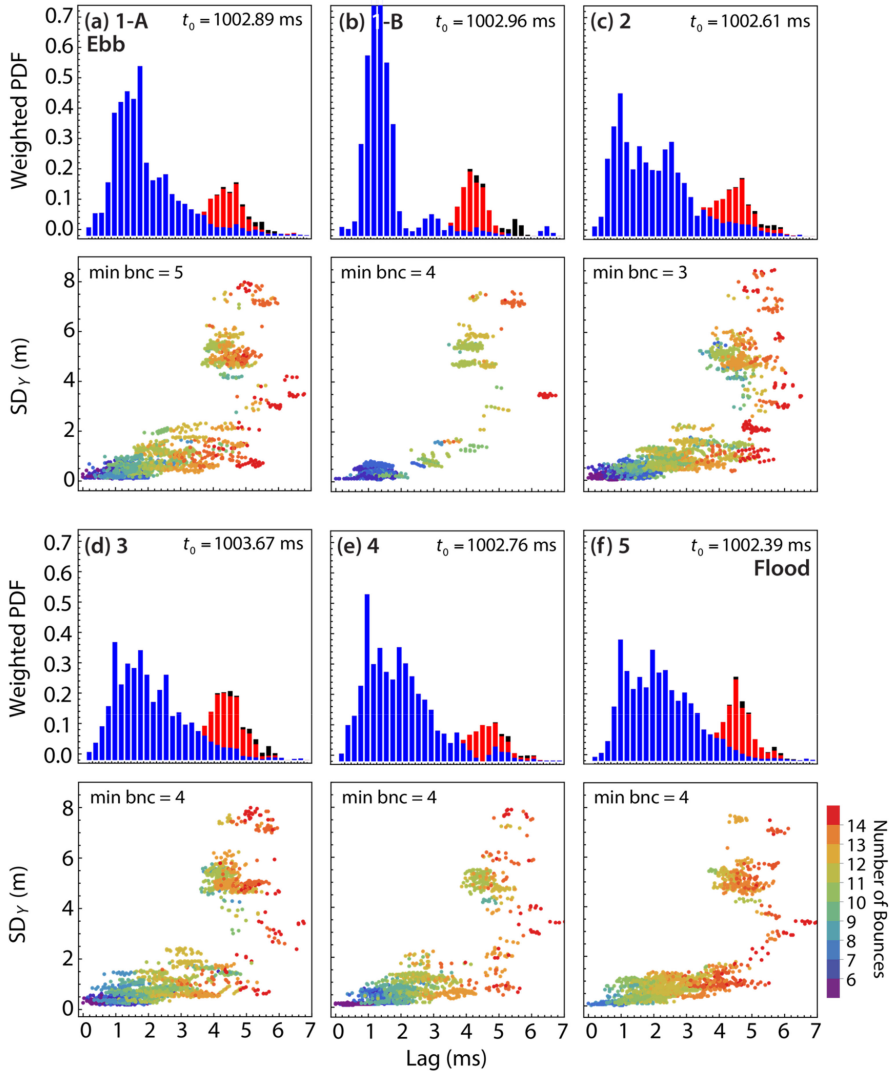

Fig. 11. Probability density function of the arrival times paired with standard deviations from the WP–FP line in the *XY*-plane, SD$_Y$ for the PDFs. The color code in PDFs corresponds to the three arrivals shown in Fig. 10. The SD$_Y$ distributions are color coded based on the number of interactions of rays with the boundaries, derived from Bellhop3D simulations. In each panel, the earliest arrival time t_0 is subtracted to give the relative lag. The minimum number of ray bounces is indicated by "min bnc."

different cases, except for case 1-B in which the horizontal fan width was constrained to 1°. In this case, even with the beamwidth reduced to 1°, we still see the three arrivals. However, the number of late arrivals increases with the beamwidth, for instance in case 1-A about 50% of arrivals have a lag less than 2 ms, whereas for case 1-B, this portion increases to 65%. A striking feature is a high correlation between the azimuthal angle and the ray length, i.e., at any given grazing angle, a slight increase in θ_{XY} toward positive values leads to a marked decrease in ray length.

The Bellhop3D results imply that multiple arrival times arise mainly due to the combined effects of bed geometry, particularly due to the concave upward bathymetry contours near the transducers, and to the finite horizontal fan width. Rays that arrive at (or pass through) two specific off-axis points close to the FP transducer contribute to the second and third arrivals irrespective of the paths that they took to get to those points. The second and third arrivals were characterized by many surface/bottom reflections and ray paths that followed more constrained paths through the channel (see Fig. 12). We suspect that the less reliable nature of these arrivals in the FAT data indicates attenuation associated with the presence of near-surface bubbles. This also means that the difference in the paths seen in the present study do not depend on water properties. Also, the paths are sufficiently similar as to sample essentially the same water, precluding any extraction of water properties from the multiple arrivals. In well-mixed conditions, such as we had in our study, adding additional acoustic nodes in the horizontal plane seems to be the only way to gain tomographic information.

VI. Path-Averaged Velocities

Reciprocal travel times allow the calculation of sound speed using (4), yielding the values of c_m presented in Fig. 14(a). In principle, the actual path length along a ray, Γ, may differ slightly from the straight-line distance L. To evaluate this difference, we used the Bellhop3D results derived for a water depth of

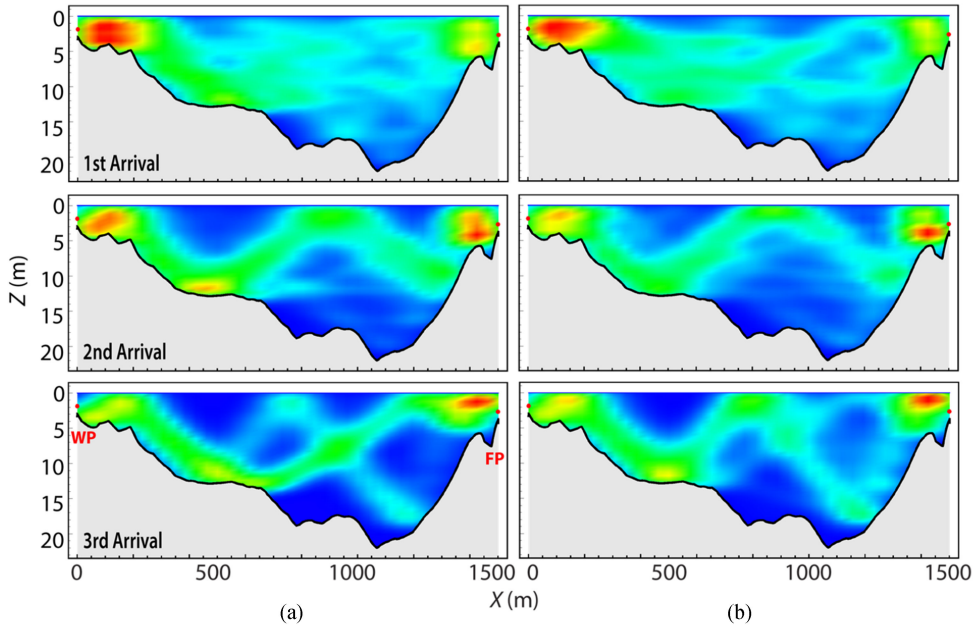

Fig. 12. Relative density of rays in the *XZ*-plane for (a) case 1-A (typical ebb) and (b) case-5 (typical flood). Warm (cold) colors denote high (low) values. Note how different groups of rays sample different domains and the corresponding patterns remain largely unchanged between the flood and the ebb.

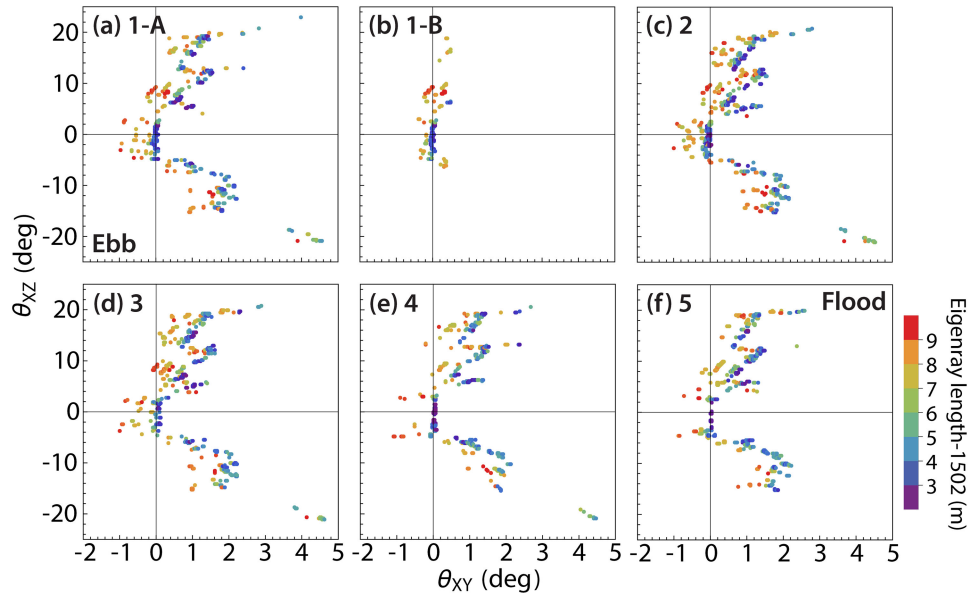

Fig. 13. Ray length as a function of the azimuthal θ_{XY} and grazing θ_{XZ} angles from Bellhop3D output. The grazing angle is zero at horizontal and positive (negative) toward the surface (bottom); azimuthal angle is zero along the WP—FP line and is positive (negative) toward the north (south). (a) 1-A. (b) 1-B. (c) 2. (d) 3. (e) 4. and (f) 5.

27.5 m (with respect to the deepest point in the channel). By applying the difference between Bellhop3D predicted mean arrival times and those directly observed, we estimated $\overline{\Gamma}_1 = 1507.5$, $\overline{\Gamma}_2 = 1509.3$, and $\overline{\Gamma}_3 = 1510.5$ m. The subscripts denote the order of arrivals and the overbar stands for averaging over all the rays within each bundle. Time series of sound-speed $c_m(\tau)$ were computed from the three coherent arrival times. As expected, the FAT-derived c_m time series in Fig. 14(a) are comparable because of the well-mixed nature of the water column. The rms values of the difference between the acoustically derived sound speeds and the values of c_{ST} estimated from the CTD and TP sensors are 0.61, 0.71, and 0.66 m/s, for the first to the third arrivals, respectively.

The path-averaged component of current was calculated from (3) for each of the three stable arrival times obtained from the FAT records together with the mean path lengths mentioned above and the corresponding $c_m(\tau)$ values shown in Fig. 14(a). The equivalent streamwise velocities, u_1, u_2, and u_3, were also

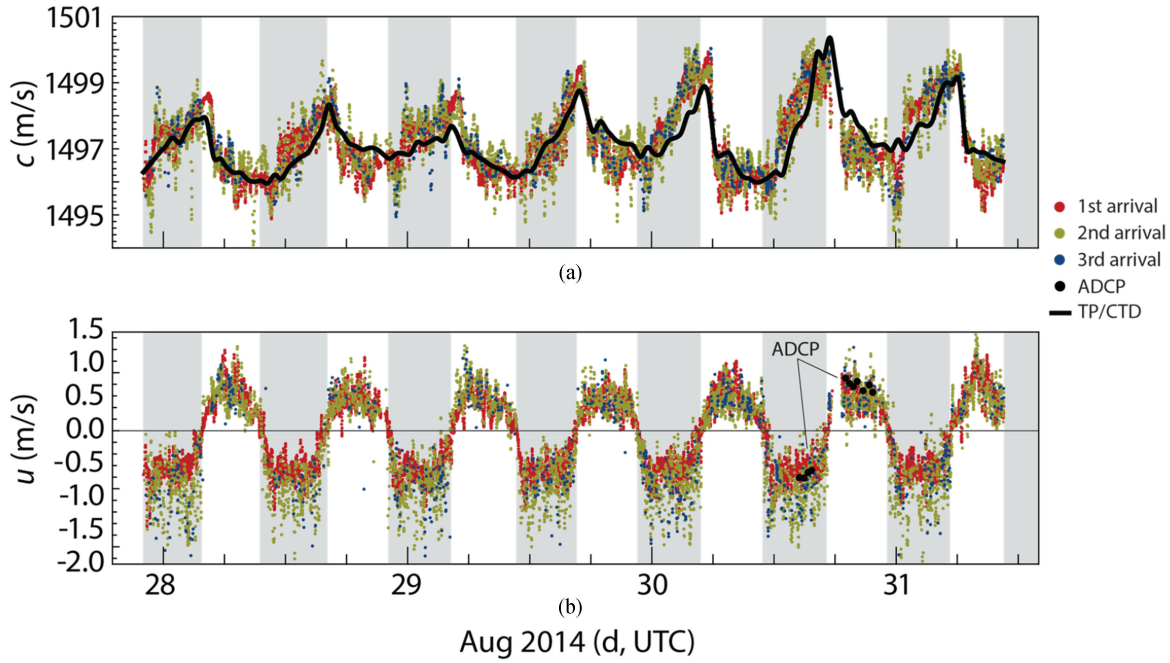

Fig. 14. (a) Sound-speed time series obtained from the three coherent arrival times low-pass filtered with 5-min cutoff period. The solid black line is $\langle c_{ST} \rangle$ from Fig. 3(c). (b) Mean streamwise currents were obtained from the three coherent arrival times low-pass filtered with 5-min cutoff period. Current speeds directly observed with the vessel-mounted ADCP averaged over the length of each transect are also shown. The gray shadings indicate flood intervals.

computed using the section-average current directions obtained from the vessel-mounted ADCP, assuming that the current direction remained unchanged through the ebb or the flood, as shown in Fig. 14(b). The current speed estimates from all three arrivals consistently indicate a well-defined semidiurnal cycle with the flood/ebb asymmetry. Based on the first arrival times, peak current speed was ca. 1.7 m/s during the flood, and 1.4 m/s during the ebb. Currents during a flood are characterized by steep increases and decreases at the start and end of the phase and a relatively constant velocity in between, whereas in the ebb, the overall tendency is a gradual increase in the current speed to reach a peak that is followed by a gentle decay to zero through the remainder of the ebb. The prominent ridge to the north of the WP–FP line extends into the channel and is the main source of eddies and macroscale turbulence advected across the WP–FP line during the ebb. There are several factors contributing to the high-frequency fluctuations seen in the currents shown in Fig. 14(b). These are pursued in the next section.

Table III lists the relative differences among the three sets of velocities derived from FAT and from direct ADCP observations. Despite the fundamental differences between the two measurement techniques, the FAT velocities derived from the first arrivals and the ADCP differ on average by less than 10%, consistent with previous works [14], [15], [35]. The mean difference for velocities obtained from later arrivals increases to 15%. Ray-tracing results from the Bellhop3D simulations (see Fig. 12) raise the possibility that the larger discrepancy between $u_2 - u_3$ and the ADCP might be due to the propagation pattern of the ray bundles corresponding to the later arrivals.

The comparison among the velocities derived from the three arrivals given in Table III implies that typically there is better

TABLE III
DIFFERENCE BETWEEN CURRENT SPEEDS ESTIMATED FROM THE THREE STABLE ARRIVALS (MARKED BY 1,2,3) AVERAGED OVER AVAILABLE DATA IN THE FLOOD (F) AND EBB (E)

	Tidal Phase	u_1	u_2	u_3
u_1	F	-	-22	-25
	E	-	2	3
u_2	F	22	-	1
	E	-2	-	4
u_{ADCP}	F	-9	15	10
	E	-8	-12	-15

FAT comparisons against ADCP data are averaged over the time it took to complete each transect. All the differences are in % and normalized against the value shown in the first column, e.g., $(u_{\mathrm{ADCP}}\text{-}u_2)/u_{\mathrm{ADCP}}$.

conformity among u_1, u_2, and u_3 during ebb than during the flood. To further investigate the differences between u_1 and u_2 during the flood and ebb, the standard deviations, SD_{u_1} and SD_{u_2}, of 15-min subsets (with no overlap) are presented in Fig. 15 (we do not include u_3 in this comparison because of the limited number of third arrivals). Also shown are the representative SNRs extracted from the signal correlations. While SD_{u_1} does not show any dependence on tidal variability, there is a clear semidiurnal signature in SD_{u_2}, with higher values during the flood than during the ebb. The SNRs corresponding to the first and second arrivals are very similar and do not follow any discernable pattern related to the tide, which indicates that increased noise is not the cause of the higher values of SD_{u_2} during the flood. We suspect that this result as well as the higher

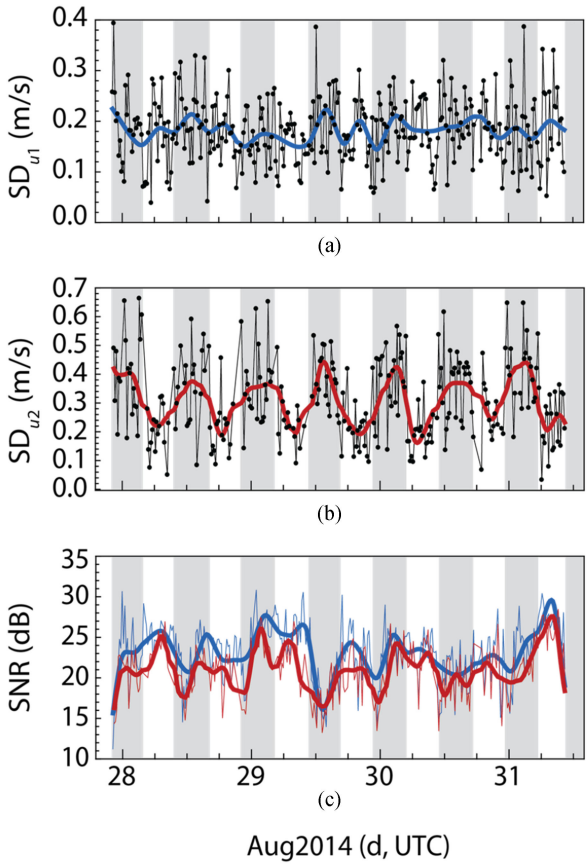

Fig. 15. Standard deviations of 15-min subsets of velocities derived from the (a) first and (b) second arrivals. (c) Same as (a) and (b) but for the corresponding representative SNR values computed from the signal correlations. The thick lines in each panel denote fluctuations after passing through an LPF with a 6-h cutoff period. The gray shadings indicate flood intervals.

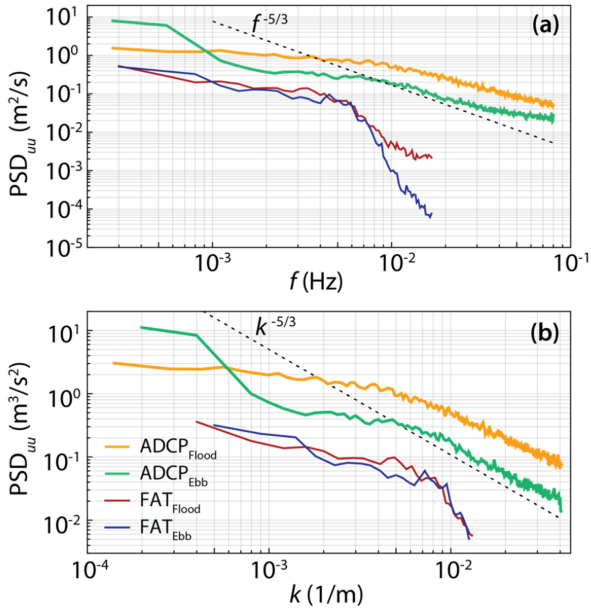

Fig. 16. Power spectral density computed for flood and ebb velocities extracted from the first arrivals registered by FAT and for the vertically-averaged along-channel velocity from the stationary ADCP as a function of (a) frequency and (b) cyclic wave number. In panel (b), the noise level was removed before converting frequency to cyclic wave number.

speeds seen during the flood for second arrivals (see Table III) is a consequence of the more selective spatial sampling realized by later arrivals. In Fig. 12, we see that the second arrivals preferentially sample the surface from the middle of the channel making it possible that higher speeds during the flood in this area could explain the observed differences. Also, from separate field observations, we know that bubble plumes penetrate closer to the bottom during the flood than during the ebb. Perhaps, the presence of these bubbles interfering with near-surface ray paths would impact values of SD_{u_2} much more than SD_{u_1}.

VII. Velocity Spectra

The velocity time series in Fig. 14 indicate that tidal-frequency variations are well resolved in the FAT data, but provide little insight into the variability of the flow at higher frequencies. Power spectra of flow velocities during the flood and the ebb were derived from the first arrivals and these are shown in Fig. 16. These spectra were calculated using 120-data-point (1 h) detrended ensembles, smoothed with a Kaiser window (parameter value of 3) and 61.9% overlap between the data subsets. Only ensembles with mean velocities greater than 0.5 m/s are included. This choice of velocity threshold implies that the spectra are representative of conditions during the full flood and the full ebb [see Fig. 14(a)]. The mean flow speeds averaged over all selected segments were 0.69 and 0.63 m/s for the flood and the ebb, respectively, the higher value during the flood again reflecting the flood/ebb asymmetry of the flow in Grand Passage. Also shown in Fig. 16 are the ensemble-averaged spectra of the vertically-averaged along-channel component of the flow computed from the bottom-mounted ADCP data during the full flood and the full ebb. The vertical average is over the 1-m to 9.5-m vertical range interval [the minimum height of the water column above the instrument was 11.4 m (flood) and 12.6 m (ebb)]. The ensemble-mean vertically-averaged velocities were 1.95 m/s and 1.41 m/s for the flood and the ebb, respectively. The spectra were computed using 1 h long, detrended, Hanning-windowed segments, with 50% overlap between consecutive segments. Times of high surface wave activity associated with storm events, identified by high variance in the bottom pressure, were excluded from the ensemble averages. The flood (ebb) spectra in Fig. 16 represent the average of the spectra for 81 (95) 1-h segments. The ADCP spectra in Fig. 16(a) have been truncated at 0.08 Hz, well below the 1-Hz Nyquist frequency and the $>$ 0.1 Hz wind-wave band, because the interest here is in comparison with the frequencies spanned by the FAT spectra.

Fig. 16(b) shows the frequency spectra transformed to wave number space by invoking Taylor's frozen turbulence hypothesis after removal of the noise floor. The ADCP noise variance is given by $\sigma_N^2 = \sigma_V^2/(N \sin\theta)$, where σ_V is the manufacturer-specified single-ping beam velocity precision, N is the number (18) of range bins included in the vertical average, and θ is

the 25° depression angle of the slant beams. The corresponding noise spectral density σ_N^2 divided by the Nyquist frequency is 0.012 m^2/s. This noise level was verified by comparison to the mean spectral densities above 0.8 Hz at low flow speeds (see [27], [36], [37] for validation of this approach). The FAT noise floor was based on the ensemble-averaged variance at mean speeds below 0.03 m/s, yielding a value of 3.19×10^{-4} m^2/s, with no dependence on the tidal phase. The ADCP spectra in Fig. 16(b) exhibit the -5/3 roll-off characteristic of inertial subrange turbulence, as expected based on previous studies of turbulence in Grand Passage [27], [36], [37]. However, the $-5/3$ slope begins at $k \sim 10^{-2}$1/m, corresponding to spatial scales greater than 100 m. This scale is an order of magnitude larger than the approximately 10-m values indicated by the above-cited studies and is attributed to the use here of vertically-averaged velocities. Velocity spectra at any given height above the bottom indicate that the upper limit of the turbulence production range in Grand Passage occurs at a wave number of about 0.1 1/m, corresponding to a spatial scale comparable to the water depth. In contrast, the spectra in Fig. 16(b) indicate that the production of vertically-averaged turbulence occurs at much larger scales.

At wave numbers below 4×10^{-3}1/m, the spectra from both FAT and the ADCP exhibit a gentle increase in variance density as wave number decreases, with comparable slopes. The FAT spectral densities are lower than those for the ADCP, by almost an order of magnitude. The ADCP levels are high because the vertically-integrated velocity from the ADCP represents a point measurement in mid-channel (see Fig. 9) where the flow speeds and turbulence levels are inherently higher than at other cross-channel locations. The FAT levels are low because ray paths span the full width of the channel and, therefore, include the lower speed, shallower areas on the channel sides, particularly the west side [see Figs. 4(a) and 9]. The ADCP spectra exhibit a pronounced flood/ebb asymmetry, with higher levels during the flood. The flood/ebb asymmetry in the flow and turbulence levels in Grand Passage is a known result and has been attributed to differences in upstream bathymetry and bottom roughness as well as flood/ebb differences in mean speed along the channel axis [27]. The sense of the asymmetry—i.e., whether the flood or the ebb is higher—varies from location to location in the channel because the upstream channel geometry and bottom roughness change with location [27]. It is, therefore, unsurprising that similar asymmetry is not evident in the FAT spectra since, at any given cross-channel position, upstream bottom roughness and bathymetry are necessarily different, and these differences average out along the FP–WP line (see Fig. 9). The FAT mean speeds at the full flood and the ebb, 0.69 and 0.63 m/s, respectively, are lower and less asymmetric than those for the ADCP (1.9 and 1.4 m/s) for the same reason. Finally, only the larger eddies along the 1.5-km path can influence the observed travel time, since the contributions of small-scale eddies to the net travel time—i.e., to the summation $t = \sum \ell_i/(c \pm v_i)$ where ℓ_i and v_i are the size and velocity of the ith eddy—will necessarily average out. The sharp roll-off in the FAT spectra near $k = 0.01$ /m is due to an artifact of velocity estimate processing and indicates that the smallest eddies that could be resolved during the 2014 experiment were O(100 m) in horizontal scale.

VIII. Discussion

The physical oceanographic conditions at our survey site are similar to those of Taniguchi *et al.* [38]—a tidal strait with a depth of approximately 50 m and currents as fast as 2 m/s—therefore, it is relevant to compare the two studies. Taniguchi *et al.* [38] used a 13-kHz CAT system with two acoustic nodes 2842 m apart to perform burst reciprocal sampling (6 samples spaced 1-min apart in 10-min intervals). They show that the high-frequency variance in velocity measurements is consistent with the code bit length. Non-tidal oscillatory velocity variations with 2–3-h periods were observed, which the authors suggested may have been caused by seiching. The high angle of their transmission path to the main flow (near perpendicular) would have eliminated most of the tidal current signal and indicates that their measurements mainly reflect characteristics of the cross-channel velocity component. In contrast, in the present study, during the flood (ebb), the transmit–receive path was at an angle of about 68.5° (30.1°) relative to the mid-channel mean flow direction, so the measurements are equally sensitive to both horizontal velocity components. While we also observe high-frequency variability in the flow, there is no evidence of periodic variations at supra-tidal frequencies, and we attribute this variability to macroscale turbulence.

In Grand Passage, we observed consistent multiple arrivals and used Bellhop3D to explain their origin through out-of-plane propagation patterns. However, in [38] the multiple arrivals did not seem to have the consistent stability that was evident in the Grand Passage data and their 2-D ray-tracing model, based on [39], was unable to simulate the number of arrivals correctly. Consequently, their treatment of the multiple arrivals was concerned with the added uncertainty in velocity measurements and not with the nature of the flow variability as in the present work.

IX. Summary and Conclusion

Results are presented from a 4-day shallow water acoustic tomography experiment in Grand Passage, NS, Canada, using two 7-kHz transducers to make reciprocal sound transmissions along a 1.5-km path. The deepest point of the channel at high water was approximately 30 m, with tidal currents as high as 1.7 m/s during the observations. Due to the channel geometry, a shoreline-trapped eddy developed near the WP station during the ebb, creating a localized pool of warmer water and a temperature front in the mid-channel. This front was not present during the flood.

Interpretation of the tomography data is complicated by the presence of multiple arrivals. By examining the difference between each succeeding arrival time with the corresponding times in the reverse transmission direction, we eliminated the possible role of horizontal shear in inducing multiple arrivals. The Bellhop3D suite was used to explore the influence of other factors including bathymetry, horizontal and vertical gradients of sound-speed, and the horizontal width of the sound beam on the propagation of sound along multiple stable arrivals. Overall, the simulation results indicate that the three primary

multiple arrivals are associated with the separation of the ray paths into three distinct bundles. These paths are caused by out-of-plane scattering associated with the upward concave form of bathymetry close to the transducers. In particular, a shoal on the FP side of the channel tended to reflect rays so as to create two additional distinct arrival paths. A transmitted beam fan of only 1° in the horizontal was sufficient to give rise to three distinct arrivals. A wider beam fan did lead to increased numbers of arrivals in all observed paths because multiple bottom interactions served to channel additional ray paths so that they would strike the FP shoal at the necessary location. The variability in arrivals demonstrated in Fig. 10 is possibly due to subtle changes in temperature and the occurrence of near-surface bubbles impacting ray path stability. In general, the presence of multiple arrivals could provide the potential for the interpretation of oceanographic processes. However, in this study, the origins of the multiple arrivals were due to out-of-plane bottom reflections and so their presence provided no information specific to the temperature structure. If the distinct paths sampled separate water volumes that might have provided information but the path separations were of such small displacements (less than 25 m in *XY*-plane), they provide no information on the spatial structure of the flow.

Path-averaged currents were estimated from the three coherent arrival times identified in the reciprocal transmissions. The 11 moving-vessel ADCP transects provided baseline information to determine which of the arrivals yield a more accurate estimation of current in the channel. Despite unreliable measurements of current from the sparse third arrivals (only 9% of reciprocal transmissions contained the third arrival), the first consistent arrivals estimated flow with less than 10% relative deviation from ADCP data. There were notable differences in speeds and standard deviations extracted from the first and subsequent arrivals (Appendix A describes instrumentation sources of velocity measurement error, which are small compared to actual current variability). The first arrival provides a fairly uniform sampling of the channel while the late arrivals have more restricted sampling patterns (see Fig. 12). We suspect that differences in speed measurements are caused by spatial structure in the velocity field and differences in how the presence of bubble plumes might affect the various ray paths. Much finer sampling resolution either with additional shore stations or supplemental field observations would be needed to fully explain these differences or to extract tomographic environmental information from them.

Velocity spectra from the FAT system are compared with those made using depth-averaged measurements from a moored ADCP. While the sampling scales of the two instruments are very different, the spectral slopes compare favorably at wave numbers between 4×10^{-3} and 8×10^{-3}1/m. The steep roll-off at wave numbers above 10^{-2}1/m in FAT spectra are caused by signal processing methods and impose a scale of O(100 m) to the smallest eddies that could be resolved along the 1.5-km path.

The good agreement between the channel-averaged currents from the vessel-mounted ADCP and those from the first and second arrivals from FAT demonstrate the potential of shallow water acoustic tomography for monitoring flow conditions in highly turbulent tidal channels. Similarly, the good agreement between the tomographic estimates of sound speed (which depends mainly on temperature here) and those obtained from in-situ temperature data indicates the potential of shallow acoustic tomography for monitoring temperature on tidal and subtidal time scales. Important advantages of shore-based tomographic systems compared to multiple ADCP deployments are lower cost and simpler deployment logistics, real-time access to the data, and channel-wide coverage. In this feasibility study, a single transmit/receive transducer pair was used. The relatively low cost of the system would allow for the implementation of multiple pairs in an array to resolve large-scale structures in the flow and sound-speed fields, like the shore-trapped eddy in Grand Passage. The m-sequence coding is a proven and effective technique for suppressing random noise. Evidence of its effectiveness in this project is the fact that the data were not affected by noise from the ferry. Thus, shallow water acoustic tomography offers a number of advantages for long-term monitoring of flow in tidal channels and could be of substantial benefit to the tidal power industry as it moves toward the deployment of turbine arrays and long-term operations.

Appendix A
Uncertainties in Streamwise Velocity Estimates

Uncertainty in streamwise velocity estimates will be introduced by errors in the assumed flow geometry (angularity errors) and by uncertainty in the length of the various acoustic paths.

We can explore the significance of the angularity errors by considering the component of the measured velocity. Given that the streamwise current is derived from

$$u = \frac{u_m}{\cos\gamma} \tag{6}$$

where γ is the angle between u and u_m, the relative error in the mean current caused by the uncertainty in direction measurements $\delta\gamma$ is expressed as

$$\frac{\delta u}{u} = \tan\gamma\delta\gamma. \tag{7}$$

Thus, during the flood with $\gamma\approx58°$, variability in the exact value of γ leads to larger errors in streamwise velocity compared to those made during the ebb through which $\gamma\approx18°$. In general, this angularity error could be addressed by using two pairs of transceivers with crossing paths [14], but this correction was not available in the present trial. The Bellhop3D results indicate that the rays forming the second and third arrivals deviate from the WP–FP line in the horizontal plane by 0.5°–1°, whereas the first arrivals traverse the cross-section directly along the line. Therefore, the rays contributing to the late arrivals make a slightly different angle with the mean current leading to larger Δt values than the first arrivals [see Fig. 7(a)]. This difference is magnified by a 1/cosγ factor when computing the streamwise component of flow from (6) as we do not correct the angle γ for the out-of-plane scatter. From (7), the out-of-plane scatter may induce an additional 3% error in the current estimates from the third arrival. This will add to the uncertainties of the second and third arrivals but does not explain all of the increased differences.

Path length uncertainty will also contribute to errors in the velocity estimates. In deriving (3), we assume that $\Gamma_i = L$. However, Bellhop3D simulations indicate that the ray path length of the second/third arrivals is larger than the first arrivals mainly due to more bounces in the vertical and out-of-plane scatter in the horizontal plane. To quantify the error caused by this assumption and its contribution to the velocities derived from the first and second arrivals, and also the displacement of the transducers by currents, we take the total derivative of (3) and remove the time terms, which yields

$$\frac{\delta u_m}{u_m} = -\frac{\delta L}{L} \tag{8}$$

where δu_m is the bias in the path-averaged current induced by the difference between the actual ray paths length and horizontal distance between source and receiver, i.e., $\delta L = \Gamma_i^{\pm} - L$. Bellhop3D predicts the longest ray, with less than 20 bounces, to be $\sim$1514 m with $L = 1502$ m. Therefore, conservatively, we can assume δL $\approx$ 20 m. With $u_m = 1.5$ m/s, the maximum δu_m is $\sim$2 cm/s. The uncertainty due to the constant ray length assumption is slightly smaller in velocities derived from the first and second arrival times as the length of the rays forming the first and second arrivals are smaller than that of the third. Furthermore, the uncertainty in current measurements imposed by the intermittent movement of the transducers ($<$0.5 m) should be negligible compared to that introduced by ray length variability.

ACKNOWLEDGMENT

The authors would like to thank Prof. Arata Kaneko from Hiroshima University and Dr. Noriaki Gohda from Aqua Environmental Monitoring Limited Liability Partnership (AEM-LLP) for their strong support in constructing the acoustic system. The authors would also like to express their gratitude to Chris Stevenson for his preliminary Bellhop3D work. The raw data obtained from the FAT system, ADCP, CTD, and TP sensors are available through the Platform for Marine Research repository (http://www.vliz.be/en/imis?module=dataset&dasid=7750) that is managed by Flanders Marine Institute.

REFERENCES

[1] H. A. Deferrari and H. Nguyen, "Acoustic reciprocal transmission experiments, Florida Straits," *J. Acoust. Soc. Amer.*, vol. 79, no. 2, pp. 299–315, 1986.

[2] A. Kaneko, G. Yuan, N. Gohda, and I. Nakano, "Optimum design of the ocean acoustic tomography system for the Sea of Japan," *J. Oceanogr.*, vol. 50, no. 3, pp. 281–293, 1994.

[3] H. Zheng *et al.*, "Reciprocal sound transmission experiment for current measurement in the Seto Inland Sea, Japan," *J. Oceanogr.*, vol. 53, pp. 117–128, 1997.

[4] K. Kawanishi, A. Kaneko, M. Razaz, and T. Abe, "Measurement of cross-sectional average velocity in a shallow tidal river with a next-generation acoustic velocity meter," in *Advances in Water Resources and Hydraulic Engineering*. Berlin, Germany: Springer, 2009, pp. 1972–1977.

[5] B. Katsnelson, V. Petnikov, and J. Lynch, *Fundamentals of Shallow Water Acoustics*. Berlin, Germany: Springer, 2012.

[6] M. K. Simon, J. K. Omura, and B. K. Levitt, *Spread Spectrum Communications Handbook*. New York, NY, USA: McGraw-Hill, 1985.

[7] J. V. Sloat and W. S. Gain, Application of acoustic velocity meters for gaging discharge of three low-velocity tidal streams in the St. Johns River Basin, Northeast Florida U.S. Dept. Interior, U.S. Geological Survey, Washington, DC, USA, 1995.

[8] D. M. Farmer, S. F. Clifford, and J. A. Verrall, "Scintillation structure of a turbulent tidal flow," *J. Geophys. Res., Oceans*, vol. 92, no. C5, pp. 5369–5382, 1987.

[9] Y. Nihei and A. Kimizu, "A new monitoring system for river discharge with horizontal acoustic Doppler current profiler measurements and river flow simulation," *Water Resour. Res.*, vol. 44, no. 4, p. 15, 2008.

[10] A. Copping *et al.*, "Tethys: Developing a commons for understanding environmental effects of ocean renewable energy," *Int. J. Mar. Energy*, vol. 3, pp. 41–51, 2013.

[11] K. Kawanisi, M. Razaz, A. Kaneko, and S. Watanabe, "Long-term measurement of stream flow and salinity in a tidal river by the use of the fluvial acoustic tomography system," *J. Hydrol.*, vol. 380, no. 1, pp. 74–81, 2010.

[12] K. Kawanisi, M. Razaz, J. Yano, and K. Ishikawa, "Continuous monitoring of a dam flush in a shallow river using two crossing ultrasonic transmission lines," *Meas. Sci. Technol.*, vol. 24, no. 5, 2013, Art. no. 055303.

[13] X.-H. Zhu, A. Kaneko, Q. Wu, C. Zhang, N. Taniguchi, and N. Gohda, "Mapping tidal current structures in Zhitouyang Bay, China, using coastal acoustic tomography," *IEEE J. Ocean. Eng.*, vol. 38, no. 2, pp. 285–296, Apr. 2013.

[14] M. Razaz, K. Kawanisi, I. Nistor, and S. Sharifi, "An acoustic travel time method for continuous velocity monitoring in shallow tidal streams," *Water Resour. Res.*, vol. 49, no. 8, pp. 4885–4899, 2013.

[15] M. Razaz, K. Kawanisi, A. Kaneko, and I. Nistor, "Application of acoustic tomography to reconstruct the horizontal flow velocity field in a shallow river," *Water Resour. Res.*, vol. 51, no. 12, pp. 9665–9678, Dec. 2015, doi: 10.1002/2015wr017102.

[16] W. Munk, P. Worcester, and C. Wunsch, *Ocean Acoustic Tomography*. Cambridge, U.K.: Cambridge Univ. Press, 2009.

[17] A. Kaneko, X.-H. Zhu, and J. Lin, *Coastal Acoustic Tomography*. Amsterdam, The Netherlands: Elsevier, 2020.

[18] A. E. Hay *et al.*, "Southwest Nova Scotia resource assessment: Final report," Offshore Energy Res. Assoc., Halifax, NS, Canada, 2013.

[19] R. Mitson, "Underwater noise of research vessels: Review and recommendations," ICES Cooperative Res. Report 209, 1995, p. 61, doi: 10.17895/ices.

[20] E.Y.E. Marine Consultants, Nov. 6, 2018. [Online]. Available: http://www.eyemarine.com/vessel/joe-casey

[21] B. Martin, C. Whitt, C. McPherson, A. Gerber, and M. Scotney, "Measurement of long-term ambient noise and tidal turbine levels in the Bay of Fundy," in *Proc. Acoust.*, 2013, vol. 26, pp. 1–6.

[22] T. J. McDougall and P. M. Barker, "Getting started with TEOS-10 and the Gibbs seawater (GSW) oceanographic toolbox," SCOR/IAPSO WG, vol. 127, pp. 1–28, 2011.

[23] IOC, SCOR, and IAPSO, "IAPSO, 2010: The international thermodynamic equation of seawater–2010: Calculation and use of thermodynamic properties," in *Intergovernmental Oceanographic Commission, Manuals and Guides*. London, U.K.: UNESCO, 2010.

[24] I. Nezu and W. Rodi, "Open-channel flow measurements with a laser Doppler anemometer," *J. Hydraulic Eng.*, vol. 112, no. 5, pp. 335–355, 1986.

[25] A. Hussain and W. Reynolds, "Measurements in fully developed turbulent channel flow," *J. Fluids Eng.*, vol. 97, no. 4, pp. 568–578, 1975.

[26] D. Shepard, "A two-dimensional interpolation function for irregularly-spaced data," in *Proc. 23rd ACM Nat. Conf.*, 1968, pp. 517–524.

[27] J. M. McMillan and A. E. Hay, "Spectral and structure function estimates of turbulence dissipation rates in a high-flow tidal channel using broadband ADCPs," *J. Atmos. Ocean. Technol.*, vol. 34, no. 1, pp. 5–20, 2017.

[28] B. D. Dushaw, P. F. Worcester, B. D. Comuelle, and B. M. Howe, "Barotropic currents and vorticity in the central North Pacific Ocean during summer 1987 determined from long-range reciprocal acoustic transmissions," *J. Geophys. Res.*, vol. 99, no. C2, pp. 3263–3272, 1994.

[29] M. B. Porter, "The Bellhop Manual and User's Guide: Preliminary Draft," Heat, Light, and Sound Research, La Jolla, CA, USA, 2011.

[30] M. B. Porter and H. P. Bucker, "Gaussian beam tracing for computing ocean acoustic fields," *J. Acoust. Soc. Amer.*, vol. 82, no. 4, pp. 1349–1359, 1987.

[31] Canadian Seabed Research Ltd., "2014 Seabed Analysis for Tidal Energy Development Grand Passage, Petit Passage and Digby Gut," Digby County, NS, Canada, 2014.

[32] M. Buckingham, "Compressional and shear wave properties of marine sediments: Comparisons between theory and data," *J. Acoust. Soc. Amer.*, vol. 117, no. 1, pp. 137–152, 2005.

[33] E. L. Hamilton, "Sound velocity as a function of depth in marine sediments," *J. Acoust. Soc. Amer.*, vol. 78, no. 4, pp. 1348–1355, 1985.

[34] E. L. Hamilton, "Sound attenuation as a function of depth in the sea floor," *J. Acoust. Soc. Amer.*, vol. 59, no. 3, pp. 528–535, 1976.
[35] K. Kawanisi, M. B. Al Sawaf, and M. M. Danial, "Automated real-time streamflow acquisition in a mountainous river using acoustic tomography," *J. Hydrologic Eng.*, vol. 23, no. 2, 2017, Art. no. 04017059.
[36] A. E. Hay, J. McMillan, R. Cheel, and D. Schillinger, "Turbulence and drag in a high Reynolds number tidal passage targetted for in-stream tidal power," in *Proc. OCEANS*, San Diego, CA, USA, 2013, pp. 1–10.
[37] J. M. McMillan, A. E. Hay, R. G. Lueck, and F. Wolk, "Rates of dissipation of turbulent kinetic energy in a high Reynolds number tidal channel," *J. Atmos. Ocean. Technol.*, vol. 33, no. 4, pp. 817–837, 2016.
[38] N. Taniguchi *et al.*, "A reciprocal acoustic transmission experiment for precise observations of tidal currents in a shallow sea," *Ocean Eng.*, vol. 219, 2021, Art. no. 108292.
[39] J. B. Bowlin, J. L. Spiesberger, T. F. Duda, and L. F. Freitag, "Ocean acoustical ray-tracing software RAY," Woods Hole Oceanographic Institution, Falmouth, MA, USA, 1992.

Mahdi Razaz received the Ph.D. degree in civil and environmental engineering from Hiroshima University, Higashi–Hiroshima, Japan, in 2010.

He collaborated with Len Zedel and Alex E. Hay on SwathDop (a multibeam pulse-coherent Doppler sonar) at the Memorial University of Newfoundland, St. John's, NF, Canada. He is currently an Assistant Professor with the School of Ocean Science and Engineering, University of Southern Mississippi, Stennis Space Center, Hattiesburg, MS, USA. His research interests include shallow acoustic tomography, acoustic measurements in oceans, and natural hydrocarbon seeps.

Len Zedel received the B.Sc. and M.Sc. degrees in physics from the University of Victoria, Victoria, BC, Canada, in 1982 and 1985, respectively, and the Ph.D. degree in physical oceanography from The University of British Columbia, Vancouver, BC, Canada, in 1991.

He is currently a Professor and the Department Head for the Department of Physics and Physical Oceanography, Memorial University of Newfoundland, St. John's, NF, Canada. His research interests include ocean acoustics and acoustical measurements of physical processes.

Alex E. Hay received the B.Sc. and M.Sc. degrees in physics from the University of Western Ontario, London, ON, Canada, in 1971 and 1972, and the Ph.D. degree in physics from The University of British Columbia, Vancouver, BC, Canada, in 1981.

He is currently a Professor of Oceanography with the Department of Oceanography, Dalhousie University, Halifax, NS, Canada. His research interests include continental shelf and nearshore processes, with an emphasis on sediment dynamics and turbulence, and in the development and use of acoustic remote-sensing systems.

Dr. Hay is a Fellow of the Acoustical Society of America.

Kiyosi Kawanisi received the graduate degree and the Doctor of Engineering degree in hydraulic engineering in 1988 from Hiroshima University (HU), Higashi–Hiroshima, Japan.

He is currently a Professor with the Department of Civil and Environmental Engineering, Graduate School of Engineering, HU. He has worked in the fields of fluid mechanics and river and coastal engineering for more than 40 years. He took a patent (No. 5555904; "acoustic tomography measurement system and method") on June 13, 2014. His recent studies have focused on innovative hydro-acoustic technology: shallow-water acoustic tomography.